Simulations of a Variable Friction Device for Multi-Hazard Mitigation

Liang Cao, S.M. ASCE [1]; Simon Laflamme, A.M. ASCE [2]; Douglas Taylor [3]; and James Ricles, M.ASCE [4]

ABSTRACT

This paper investigates the performance of a novel semi-active damping device at mitigating non-simultaneous multi-hazard loads. The device, termed modified friction device (MFD), has been previously proposed by the authors. It consists of a variable friction system based on automotive drum brake technology. The device has been demonstrated in a laboratory environment, and its dynamic behavior modeled. This model is used to conduct numerical simulations on two representative structures, one short building located in Japan and the other tall building located in Boston, MA. Simulated hazards include wind, blast, and seismic loads. Various control cases are considered, including semi-active control under five different sets of control weights, as well as passive viscous and passive friction to benchmark performance. Results show that the semi-active control cases outperforms all of the other cases for the vast majority of hazards and performance indices, provided that the right control weights are utilized.

Keywords: multi-hazard, multiple hazard, variable friction, semi-active device, supplemental damping, structural control, modified friction device

INTRODUCTION

Civil infrastructures, including buildings and energy, lifeline, communication, and transportation systems, provide significant services and benefits to our communities. These systems need to be designed, constructed, and maintained to sufficiently resist the effects of service and extreme loads to ensure continuous daily operability and public safety. In particular, modern construction techniques and materials enable the construction of lighter structures that results in higher flexibility, thereby increasing wind-induced vibrations, as an example, which may create discomfort and frequent inoperability. Also, recent extreme events (e.g., hurricanes, tornadoes, gust fronts, storm surges) have demonstrated the utmost vulnerability of buildings and transportation infrastructures.

A solution to improve structural performance vis-a-vis service and extreme loads is a performance-based design (PBD) approach, by appropriately sizing structural stiffness and integrating damping systems (Connor and Laflamme 2014). The majority of the literature on PBD of civil structures heavily focusses on seismic

[1]Ph.D. Student, Department of Civil, Construction, and Environmental Engineering, Iowa State University, Ames, IA, 50011, corresponding author; email:liangcao@iastate.edu.

[2]Assistant Professor, Department of Civil, Construction, and Environmental Engineering, and Department of Electrical and Computer Engineering, Iowa State University, Ames, IA, 50011.

[3]President, Taylor Devices, North Tonawanda, NY, 14120.

[4]Bruce G. Johnston Professor of Structural Engineering, Lehigh University, Bethlehem, PA 18015.

excitations (Ganzerli et al. 2000; Stewart et al. 2002; Takewaki 2011; Trifunac 2012), but recent studies have extended the concept to multiple hazards excitation (Asprone et al. 2010; Jalayer et al. 2011; McCullough and Kareem 2011; Petrini and Palmeri 2012; Dong et al. 2013). Some of these examples conducted PBD on structures equipped with supplemental energy dissipation systems, including semi-active, hybrid, and active damping systems, here termed high performance control systems (HPCS). HPCS have been proposed due to their potential to substantially enhance structural performance in comparison with traditional passive mitigation systems, de facto reducing costs associated with structural systems and improving structural resiliency. In addition, HPCS can perform typically over a wide excitation bandwidth, ideal for a PBD approach targeting multiple hazards.

Several HPCS have been presented and demonstrated in the literature. Refs. (Connor and Laflamme 2014; Spencer Jr and Nagarajaiah 2003; Casciati et al. 2012; Ubertini 2010; Ubertini et al. 2015) provide examples of such systems. In particular, semi-active systems have gained popularity due to their high performance on low energy requirements. These devices include variable fluid, variable stiffness, variable orifice, and variable friction mechanisms. While they have shown great promise in literature (see Refs. (Casciati et al. 2012; Venanzi et al. 2013) for instance), these systems are yet to be broadly implemented. A reason is that most of the proposed damping devices do not combine mechanical robustness and high damping force (Laflamme et al. 2012a).

The authors have recently proposed a novel variable friction device termed the Modified Friction Device (MFD), as an alternative to other semi-active systems. The mechanical principle of the MFD is based on a vehicle drum brake technology, constituting a mechanically reliable mechanism, and with a theoretical maximum damping force of 200 kN (Laflamme et al. 2012b). In general, friction mechanisms combine the advantage of being 1) capable of high energy dissipation independent of velocity; 2) inexpensive; 3) easy to install; and 4) relatively low maintenance (Mualla and Belev 2002; Symans et al. 2008). However, their strong nonlinear behavior, degradation of sliding interface, possibility of cold weld, and reliance on a restoring force are strong disadvantages, most likely responsible for their lack of popularity with respect to viscous dampers. Others have proposed variable friction devices based on hydraulic (Kannan et al. 1995), pneumatic (Vesselenyi et al. 2007; Mehmood et al. 2011), electro-magnetic (Yang and Agrawal 2002; Lorenz et al. 2006), electro-mechanical (Narasimhan and Nagarajaiah 2006; Kawamoto et al. 2008)and piezoelectric (Chen and Chen 2004; Lu and Lin 2009; Durmaz et al. 2002; Xu and Ng 2008) actuators, with reported maximum frictional forces of 2 kN (Lu and Lin 2009), 3 kN (Dai et al. 2012), and 20 kN (Agrawal and Yang 2000; Narasimhan and Nagarajaiah 2006) devices.

In previous work, the authors have presented the theoretical concept of the MFD and numerically demonstrated its performance at wind mitigation over a passive energy dissipation system currently installed in a

structure located in Boston, MA (Laflamme et al. 2011a; Laflamme et al. 2012b). The authors have shown that the use of the MFD instead of a passive mitigation system could lead to savings in the order of 20% to 30% on the cost of the mitigation system. The study included the cost of the controller and maintenance. Given the promising performance of the device, a first small-scale prototype has been fabricated and tested. The characterization of its dynamic behavior is presented in Ref. (Cao et al. 2015), where a 4.5 kN capacity has been demonstrated.

In this paper, numerical simulations previously conducted on the MFD in Ref. (Laflamme et al. 2012b) are extended to different types of buildings subjected to multiple non-simultaneous hazards, which include wind, blast, and seismic events. These simulations are conducted with the device's dynamics experimentally characterized in Ref. (Cao et al. 2015) instead of the original theoretical model. The objective is to investigate the performance of the device at mitigating vibrations of different natures.

The rest of the paper is organized as follows. Section 2 gives the background on the MFD and presents its dynamic model. Section 3 describes the research methodology adopted for the investigation, which includes a description of the model buildings, loads, and control cases. Section 4 presents and discusses simulation results. Section 5 concludes the paper.

THE MODIFIED FRICTION DEVICE

The MFD is a variable friction device based on automotive dual servo drum brake systems. The drum brake technology was selected due to its high mechanical robustness and reliability, which enables the application of a predictable braking force. It also has a self-energizing mechanism, which substantially amplifies the force applied on the braking shoes. Its friction dynamic is described in Ref. (Laflamme et al. 2012b). Briefly, the device dissipates energy via friction developed by the contact of braking shoes onto a drum. Figure 1 shows the principle of the MFD. The actuation force W acts on the braking shoes to produce normal forces N_i on shoes $i = 1, 2$, which in turn generate friction forces f_i, with the total friction force $F = f_1 + f_2$. The moment produced by this friction force is counteracted by the opposite forces F_{leg} in the support legs. The geometric location of the braking shoes (parameters a, b, r) is responsible for creating a static moment, which is the self-energizing mechanism, that amplifies the actuation force by a factor C, where $F = CW$ and $C = f_c(a, b, r)$. The derivation of f_c can be found in Ref. (Mahmoud 2005).

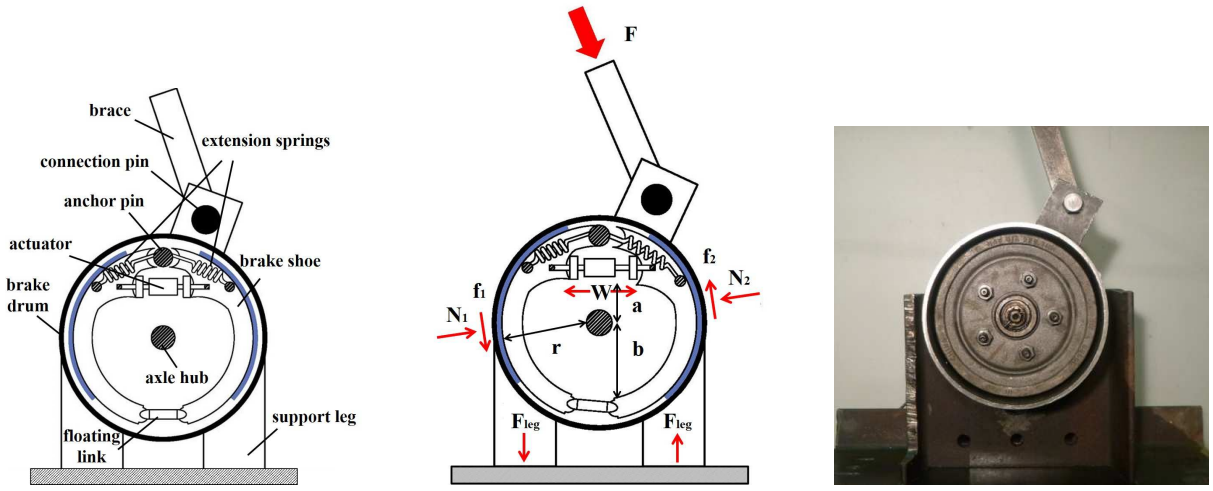

(a) (b) (c)

FIG. 1: (a) Internal components; (b) diagram of forces; and (c) picture of prototype.

Dynamic Model

The dynamics of the MFD has been characterized in a laboratory environment (Cao et al. 2015). A prototype of the MFD, shown in Fig. 1 (c), has been fabricated by directly modifying a vehicle drum brake due to the readily availability of the mechanism. The characterization process consisted of subjecting the MFD to various harmonic inputs under different actuation pressure (W was provided by a pneumatic actuator), and fitting the experimental results using a three-stage dynamic model.

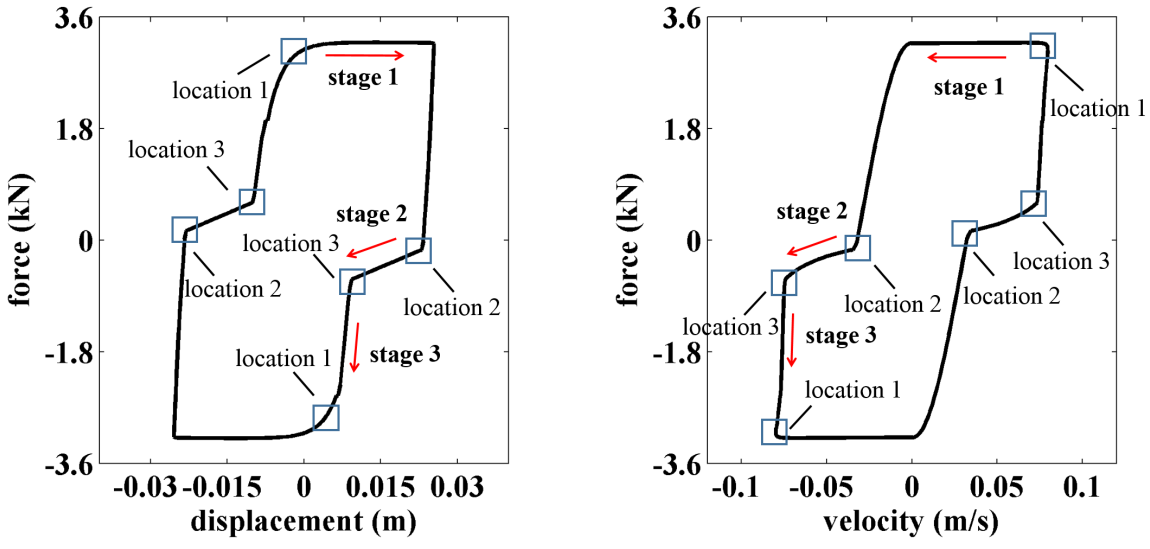

(a) (b)

FIG. 2: Dynamic model of the MFD under applied pressure of 10.34 MPa (1500 psi) : (a) force-displacement plot (0.5 Hz); and (b) force-velocity plot (0.5 Hz).

Figure 2(a)-(b) are plots of typical force-displacement and force-velocity loops from the device's dynamics, illustrating three distinct dynamic stages. Stage 1 is the typical dynamic friction mode. When the rotation of the break is reversed, there is a discontinuity in the friction force (stage 2). This is caused by the presence of a gap between the anchor pin and braking shoes, phenomenon termed backlash. Once the gap is closed, the friction force increases linearly (stage 3), until it gets back to its the typical friction dynamics.

The three-stage dynamic model is as follows:

- Stage 1 (location 1 $\longrightarrow$ location 2) - dynamic friction. The friction force F_1 is characterized using a LuGre friction model.

The force F_1 is given by

$$\begin{aligned} F_1 &= \sigma_0 \zeta + \sigma_1 \dot{\zeta} + \sigma_2 \dot{y} \\ \dot{\zeta} &= \dot{y} - \sigma_0 \frac{|\dot{y}|}{g(\dot{y})} \zeta \end{aligned} \tag{1}$$

where σ_0 represents the aggregate bristle stiffness, σ_1 microdamping, σ_2 viscous friction, ζ an evolutionary variable, y and $\dot{y}$ the tangential displacement and velocity of the device, respectively, and $g(\dot{y})$ a function that describes the Stribeck effect:

$$g(\dot{y}) = F_c + (F_s - F_c) e^{-(\frac{\dot{y}}{\dot{y}_s})^2} \tag{2}$$

where $\dot{y}_s$ is a constant modeling the Stribeck velocity, F_s the static frictional force, and F_c the kinetic frictional force.

- Stage 2 (location 2 $\longrightarrow$ location 3) - backlash. The force F_2 is taken as linear and modeled as a stiffness element k_2. This stage occurs over a drum displacement d_2.

- Stage 3 (location 3 $\longrightarrow$ location 1) - rapid increase in friction force. The force F_3 is taken as linear and modeled as a stiffness element k_3. This stage occurs over a drum displacement d_3.

A smooth transition region between these stages is provided by a C^∞ function of the type (Laflamme et al. 2011b):

$$m(y) = \frac{1}{1 + e^{-\frac{\gamma_1 (y - y_0)}{\gamma_2}}} \tag{3}$$

where y_0 is the reference displacement of the new stage, and γ_1, γ_2 are constants. For instance, the frictional force F within the transition from stage i to stage j is written

$$F = (1 - m(y))F_i + m(y)F_j \tag{4}$$

Figure 3 is a plot of a typical force-displacement loop resulting from the three-stage dynamic model described above. It is compared against a LuGre friction model. A question may arise whether the backlash phenomena may significantly affect the performance of the MFD. In particular, the effective energy dissipation ratio β of the MFD, defined as the energy dissipated by the MFD over the energy dissipated by a perfect elastic-plastic system (Iyama et al. 2009), is substantially reduced by the presence of the backlash. A study of prior research on β for structural control devices reveals that some devices with $\beta = 0.25$ performed similarly to a theoretical device with $\beta = 1.0$ (Seo and Sause 2005; Ricles et al. 2002). In addition, if a lower value for β would still be a concern, the length of the backlash is fixed. Therefore, it would be possible to increase β by amplifying structural displacements (e.g., toggle system, as discussed in the next section). Lastly, the backlash could also be reduced through alternative designs of the MFD. In the numerical simulations, the MFD performance will be compared against a pure friction device. Such comparison will enable the assessment of the effects of the backlash phenomena.

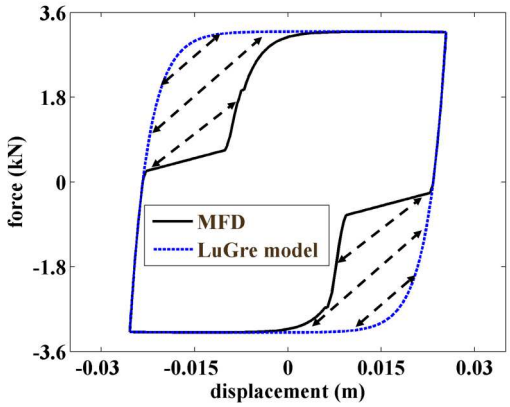

FIG. 3: MFD model (friction with backlash) versus pure friction model (friction without backlash)

Model Parameters

Tables 1 and 2 lists the values of the model parameters used for the simulations presented later.

TABLE 1: Pressure dependent parameters

parameter	stage	function
F_c	1	$F_c = C_c W$
F_s	1	$F_s = C_s W$
σ_0	1	$\sigma_0 = \alpha_{\sigma_0} W + \sigma_0\|_{W=0}$

TABLE 2: Pressure independent parameters of the MFD dynamic model

parameter	stage	value	unit
C_c	1	0.399	kip·in^{-2}
C_s	1	0.409	kip·in^{-2}
σ_1	1	1.000	psi·s·in^{-1}
σ_2	1	1.000	psi·s·in^{-1}
α_{σ_0}	1	2.000	in^{-3}
$\sigma_0\|_{W=0}$	1	3.029	kip·in^{-1}
k_2	2	0.231	kip·in^{-1}
k_3	3	3.000	kip·in^{-1}
d_2	2	0.500	in
d_3	3	0.200	in
γ_1	1-3	1.000	in
γ_2	1-3	0.100	in

Figure 4 is a plot of the force-displacement and force-velocity loops obtained from these parameters in terms of % actuation pressure (0%, 25%, 50%,75% and 100%). In the simulations, the model is scaled to a maximum friction force $F_{\max}$ obtained from the PBD procedures by selecting W such that $F_c = F_{\max} = C_c W$.

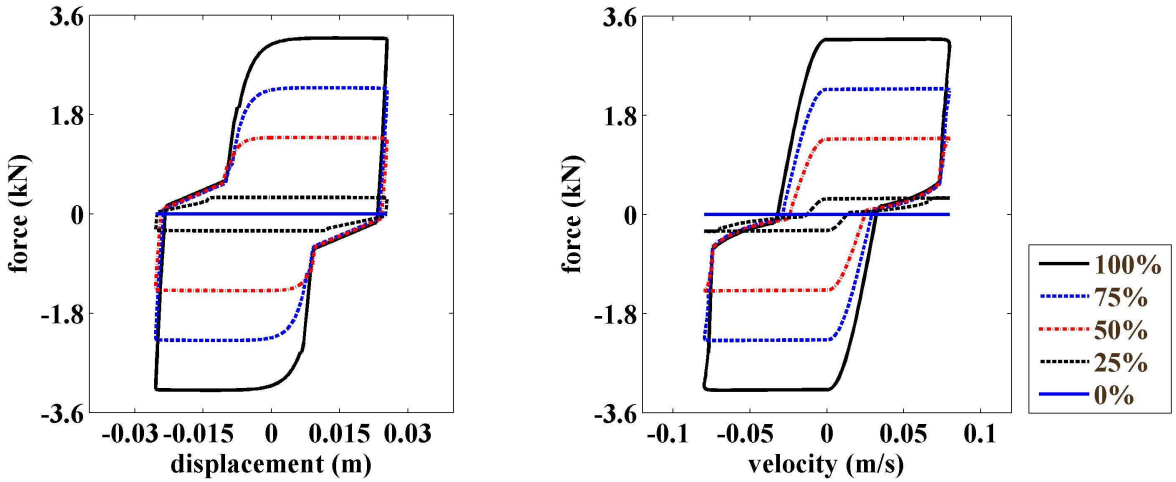

(a) (b)

FIG. 4: (a) Force-displacement and (b) force-velocity loops for a harmonic excitation of 0.0254 m (1 in) at 0.50 Hz

METHODOLOGY

State-Space Model

Consider the equation of motion of an n-story building system:

$$\mathbf{M}\ddot{\mathbf{z}} + \mathbf{C}\dot{\mathbf{z}} + \mathbf{K}\mathbf{z} = \mathbf{E_f}\mathbf{F} + \mathbf{E_u}\mathbf{u} \tag{5}$$

where $\mathbf{z} \in \mathbb{R}^{n\times 1}$ is the displacement vector, $\mathbf{F} \in \mathbb{R}^{r\times 1}$ is the control input vector, $\mathbf{u} \in \mathbb{R}^{q\times 1}$ is the external excitation input vector, $\mathbf{E_f} \in \mathbb{R}^{n\times r}$ and $\mathbf{E_u} \in \mathbb{R}^{n\times q}$ are the control and external excitation input location matrices, respectively, and $\mathbf{M}, \mathbf{C}, \mathbf{K}$ are the mass, stiffness and matrices, respectively.

The state-space representation of Eq. (5) is given by

$$\dot{\mathbf{Z}} = \mathbf{A}\mathbf{Z} + \mathbf{B_f}\mathbf{F} + \mathbf{B_u}\mathbf{u} \tag{6}$$

where $\mathbf{Z} = \begin{bmatrix} \mathbf{z} & \dot{\mathbf{z}} \end{bmatrix}^T \in \mathbb{R}^{2n\times 1}$ is state vector and the various constant coefficient matrices are defined as follows:

$$\mathbf{A} = \begin{bmatrix} \mathbf{0} & \mathbf{I} \\ -\mathbf{M^{-1}K} & -\mathbf{M^{-1}C} \end{bmatrix}_{2n\times 2n} \tag{7}$$

$$\mathbf{B_f} = \begin{bmatrix} \mathbf{0} \\ -\mathbf{M^{-1}E_f} \end{bmatrix}_{2n\times r} \tag{8}$$

$$\mathbf{B_u} = \begin{bmatrix} \mathbf{0} \\ -\mathbf{E_u} \end{bmatrix}_{2n\times q} \tag{9}$$

The notation x_i is used to denote the interstory displacement at floor i where $x_i = z_i - z_{i-1}$, except at the first floor where $x_1 = z_1$.

Controller

A sliding mode control (SMC) strategy is used to compute the required control force $\mathbf{F}_{\text{req}}$ for the MFD. The sliding surface $\mathbf{S} \in \mathbb{R}^{n\times 1}$ is taken as

$$\mathbf{S} = \mathbf{\Lambda}(\mathbf{Z} - \mathbf{Z}_d) \tag{10}$$

where $\mathbf{Z}_d$ is the desired state ($\mathbf{Z}_d \equiv \mathbf{0}$ for civil structure) and $\mathbf{\Lambda} = [\ \lambda\mathbf{I} \quad \mathbf{I}\ ] \in \mathbb{R}^{n\times 2n}$ is a user-defined weight matrix that includes strictly positive constants λ and identity matrix $\mathbf{I} \in \mathbb{R}^{n\times n}$. Consider the following Lyapunov function based on the surface error:

$$V = \frac{1}{2}\mathbf{S}^T\mathbf{S} \tag{11}$$

where V is positive definite. Taking its time derivative $\dot{V}$ yields

$$\begin{aligned}\dot{V} &= \mathbf{S}^T\dot{\mathbf{S}} \\ &= \mathbf{S}^T\mathbf{\Lambda}[\mathbf{AZ} + \mathbf{B_f}\mathbf{F}_{\text{req}} + \mathbf{B_u}\mathbf{u}] \\ &= \mathbf{Z^T}\mathbf{\Lambda^T}\mathbf{\Lambda}\mathbf{AZ} + \mathbf{S}^T\mathbf{\Lambda}[\mathbf{B_f}\mathbf{F}_{\text{req}} + \mathbf{B_u}\mathbf{u}]\end{aligned} \tag{12}$$

To ensure stability, Eq. (12) needs to be negative definite. The first term of $\dot{V}$ is negative definite, and the excitation $\mathbf{u}$ is considered as unmeasurable. Therefore, a strategy is to select required control force $\mathbf{F}_{\text{req}}$ to make the second term as negative as possible, such that $\mathbf{S}^T\mathbf{\Lambda B_f F}_{\text{req}} = -\eta\mathbf{S}^T\mathbf{S}$:

$$\mathbf{F}_{\text{req}} = -\eta([\mathbf{\Lambda B_f}]^{\mathbf{T}}[\mathbf{\Lambda B_f}])^{-1}[\mathbf{\Lambda B_f}]^{\mathbf{T}}\mathbf{S} \tag{13}$$

The required force $F_{\text{req},i}$ for device i is not necessarily attainable by the semi-active device. A bang-bang type voltage rule is adopted to attempt reaching this force, which consists of requiring a voltage $v_{\text{req},i} = v_{\max}$ when $|F_{\text{req},i}| > |F_{\text{act},i}|$ and the sign of the device velocity $\dot{x}_i$ is equal to the sign of $F_{\text{req},i}$, or requiring $v_{\text{req},i} = 0$ otherwise.

The actuation force of the break W (see Fig. 1 (b)) is taken as linear with the actual voltage v_{act}. A delay in the voltage response is assumed, such that

$$\dot{v}_{\text{act},i} = -\tau(v_{\text{act},i} - v_{\text{req},i}) \tag{14}$$

where τ is a positive constant, taken as $\tau = 200\ \text{sec}^{-1}$ based on previous simulations conducted in (Laflamme et al. 2012b).

Simulated Structures

Two different structures are selected for the simulations. They consist of a short and a tall building, located in Shizuoka City, Japan, and Boston, MA, respectively. They were selected due to their different dynamics and sites. Each structure is simulated with MFDs, and results are benchmarked against uncontrolled cases, as well as passive viscous damping and passive friction damping cases. The model of each structure, including the PBD procedures used in selecting the parameters for each set of devices, is described in what follows.

Short Building

The short building is a 5-story structure, described in Kurata et al. (Kurata et al. 1999). It is a steel moment-resisting frame with a semi-active damper system located in Shizuoka City, Japan. The structure is modeled as a lumped-mass shear system, and simulated along its weak axis using the dynamic properties listed in Table 3. Table 4 compares the values of the first three periods of the system reported in the literature (Kurata et al. 1999) to the numerical model, and lists their effictive modal mass Γ.

TABLE 3: Dynamic properties of short building model

floor	mass (kg)	stiffness (kN/m)	damping (kN·s/m)
5	266100	84000	530
4	204800	89000	562
3	207000	99000	625
2	209200	113000	713
1	215200	147000	928

TABLE 4: Fundamental periods and comparison of short building

period	report (s)	model (s)	difference (%)	Γ (%)
first	0.992	0.991	−0.01	82.81
second	0.354	0.354	0.00	11.15
third	0.222	0.223	+0.27	3.68

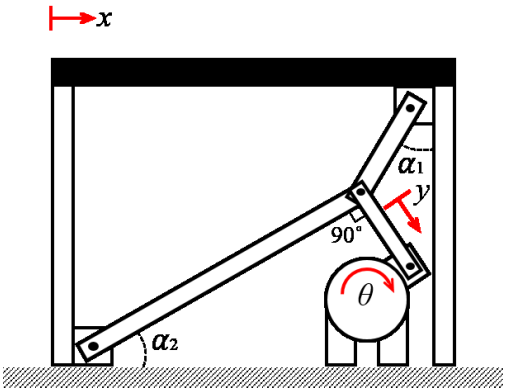

FIG. 5: Toggle configuration of MFD placement within bracing systems

The simulated damping devices are assumed to be installed with toggle braces within each floor, as illustrated in Fig. 5. The toggle system is used to amplify the inter-story displacement x, resulting in an amplified rotational displacement θ (Constantinou et al. 2001):

$$\theta = \frac{\sin\alpha_1}{\cos(\alpha_1 + \alpha_2)} xr \tag{15}$$

where r is the radius of the drum, and $y = \theta r$ is the tangential displacement of the drum. The derivation of Eq. (15) assumed small inter-storey drift.

The following PBD methodology has been adopted for the selection of the devices' parameters (e.g., maximum damping force and viscous constant). The damping matrix $\mathbf{C}$ is assumed to be proportional to the stiffness matrix $\mathbf{K}$:

$$\mathbf{C} = \alpha_0 \mathbf{K} \tag{16}$$

where α_0 is the proportionality constant. A viscous damping ratio ξ_j is prescribed for mode j, α_0 is determined by the following equation (Connor and Laflamme 2014):

$$\alpha_0 = \frac{2\xi_j}{\omega_j} \tag{17}$$

where ω_i is the frequency of mode j. Assuming dampers of constant coefficients c_i installed at each floor, it can be shown that the coefficient c_i is given by the following relationship:

$$c_i = \alpha_0 k_i \tag{18}$$

For the simulations, the damping ratio for the first mode ($j = 1$) is assumed to be 2% for the uncontrolled case, and a target design of 10% for the controlled cases to provide conservative values on the relative performance of the control system (Connor and Laflamme 2014). The friction capacity of each MFD is determined by equivalent viscous damping to compare with the viscous devices

$$F_{i,\max} = \frac{c_i \pi \Omega x_i}{4} \tag{19}$$

where Ω is the frequency response of the structure and $F_{i,\max}$ is the MFD maximum capacity at floor i. The maximum damping capacity of each viscous damper is then set equal to $F_{i,\max}$. The MFD is arbitrarily designed for a harmonic excitation acting at the structure's fundamental frequency ω_1, with $\Omega = \omega_1$. The selection of x_i is based on an assumed design story drift of 2% based on allowable story drift in ASCE 7-10 (table 12.12-1) (ASCE 2013) for wind loads. The resulting configuration for each device type is listed in Table 5, where N_i is the number of devices at floor i.

TABLE 5: Damper configuration for short building

floor	story height	$F_{i,\max}$	c_i	N_i
	m	kN	(kN·s/m)	
5	3.6	263	441	2
4	3.6	280	468	2
3	3.6	310	520	2
2	3.6	353	593	2
1	4.2	461	773	2

Tall Building

The tall building is a 39-story office tower located in downtown Boston, MA. The structure is modeled as a lumped-mass shear system, and simulated along its weak axis using the dynamic parameters reported in (Laflamme et al. 2011a) and listed in Table 6 (Mcnamara and Taylor 2003). The weak direction of the structure was selected because it is currently equipped with toggles and viscous damping devices.

TABLE 6: Dynamic properties of tall building model

floor	mass (t)	stiffness (kN/m)	damping (kN·s/m)	floor	mass (t)	stiffness (kN/m)	damping (kN·s/m)
39	125	13206	194	19	948	1414101	20481
38	903	61570	915	18	948	1542103	22332
37	984	144156	2112	17	948	1671516	24204
36	804	200943	2928	16	948	1704402	24680
35	948	429995	6246	15	948	1736539	25145
34	948	668236	9692	14	948	1848105	26758
33	948	688855	9990	13	948	1954807	28302
32	948	707994	10267	12	948	1987942	28781
31	948	721919	10468	11	948	2024855	29315
30	948	788614	11433	10	948	2283559	33057
29	948	866126	12554	9	948	2536604	36717
28	948	880965	12769	8	948	2579392	37336
27	948	889946	12899	7	948	2615282	37855
26	948	959764	13909	6	1482	2662444	38552
25	948	1030839	14937	5	1394	3226434	46708
24	948	1049684	15209	4	1394	3919347	56731
23	948	1064386	15422	3	2295	3929345	56900
22	948	1216929	17620	2	3150	2751949	39892
21	948	1370469	19849	1	1671	2193660	31776
20	948	1385321	20064				

Table 7 compares the values of the first three periods of the system reported in literature (Mcnamara and Taylor 2003) to the numerical model, and lists their effective modal mass Γ.

TABLE 7: Fundamental periods and comparison of tall building

period	reported (s)	model (s)	Difference (%)	Γ (%)
first	5.00	5.00	0.00	64.03
second	1.82	2.07	−13.7	13.20
third	N/A	1.39	N/A	7.10

The structure is currently equipped with passive fluid viscous dampers at every other floor to mitigate wind-induced vibrations. These dampers provide a supplement damping ratio of 3% (McNamara et al. 2000). The simulated passive viscous case uses the design parameters of the existing damping system (Mcnamara and Taylor 2003; Laflamme et al. 2012b). The simulated MFDs are installed at the same locations as for the passive system, within a toggle brace element. The same PBD methodology as for the short building is adopted for selecting the maximum damping forces of the MFDs and the viscous dampers, for which the MFDs are designed to provide an equivalent damping of 3%. The resulting configuration for each device type is listed in Table 8.

TABLE 8: Damper configurations for tall building

floor	$F_{i,\max}$ (kN)	c_i (kN·s/m)	N_i
above 26^{th} floor	135	1750	8
below 26^{th} floor	270	3500	22

Simulated Loads

Each structure is simulated under various hazards. They include two wind events, one blast event, and six seismic events. The methodology used to simulate each hazard is described in what follows.

Wind Loads

A variable wind speed model is used to generate the wind speed time series data at the top story of the simulated building based on the literature (Slootweg et al. 2003). A wind speed time series $\nu_{w,\text{top}}(t)$ is modeled as

$$\nu_{w,\text{top}}(t) = \nu_a + \nu_r(t) + \nu_g(t) + \nu_t(t) \tag{20}$$

where ν_a is the average wind speed, ν_r the wind speed ramp, ν_g the wind gust, and ν_t the wind turbulence. The wind speed ramp is taken as

$$\nu_r(t) = \begin{cases} 0 & \text{if} \quad t < T_{\text{sr}} \\ \nu_{\text{ramp}}(t) & \text{if} \quad T_{\text{sr}} < t < T_{\text{er}} \\ 0 & \text{if} \quad t > T_{\text{er}} \end{cases} \tag{21}$$

where $\nu_{\text{ramp}}(t) = A_{\text{ramp}} \frac{t - T_{\text{sr}}}{T_{\text{er}} - T_{\text{sr}}}$ and A_{ramp} is the amplitude of wind speed ramp, T_{sr} and T_{er} are the starting and end time of the wind speed ramp, respectively. The wind speed gust is characterized by

$$\nu_g(t) = \begin{cases} 0 & \text{if} \quad t < T_{\text{sg}} \\ \nu_{\text{gust}}(t) & \text{if} \quad T_{\text{sg}} < t < T_{\text{eg}} \\ 0 & \text{if} \quad t > T_{\text{eg}} \end{cases} \tag{22}$$

where $\nu_{\text{gust}}(t) = A_{\text{gust}}(1 - \cos(\omega_g(\frac{t-T_{\text{sg}}}{T_{\text{eg}}-T_{\text{sg}}})))$, with A_{gust} being the amplitude of the wind speed gust, ω_g a constant, T_{sg} and T_{eg} the starting and end time of wind speed gust, respectively. The wind speed gust is a periodic time series that can be tuned to a specific frequency. Under the classic assumption of modeling wind turbulence as a zero-mean Gaussian stochastic process, time domain realizations are generated by the waves superposition formula (Shinozuka and Jan 1972; Ubertini and Giuliano 2010):

$$\nu_t(t) = \sqrt{2}\sum_{k=1}^{N}[P_D(\omega_k)\Delta\omega]^{\frac{1}{2}}\cos(\omega_k t + \phi_k) \tag{23}$$

where ω_k is the frequency (Hz), ϕ_k is a random phase uniformly distributed between 0 and 2π and $P_D(\omega_k)$ is the power spectral density function of wind turbulence (Slootweg et al. 2003)

$$P_D(\omega_k) = l\nu_a\left(\ln\left(\frac{h}{z_0}\right)^2\right)^{-1}\left(1 + 1.5\frac{\omega_k l}{\nu_a}\right)^{-5/3} \tag{24}$$

where h is the height from the ground (m), l is the turbulence length scale (m) and z_0 is the roughness length (m) that can be determined from Ref. (Mendis et al. 2007). In Eq. 24, the wind spectrum is discretized using N_ω equally spaced frequency points, $\omega_k = k\Delta\omega$, with a frequency step amplitude $\Delta\omega$ and a cutoff frequency $\omega_c = N_\omega\Delta\omega$.

The wind speed distribution on each building follows a power law

$$\nu_{w,i}(t) = \nu_{w,\text{top}}(t)\left(\frac{h_i}{h_{\text{top}}}\right)^{\varphi} \tag{25}$$

where φ is a constant taken as 0.143 (Hsu et al. 1994), $\nu_{w,i}(t)$ is the wind speed at story i of height h_i, and $\nu_{w,\text{top}}$ is the reference wind speed at the top story of height h_{top}. The value $\nu_{w,\text{top}}(t)$ is generated from Eq. 20 and the wind speeds at the other stories are calculated based on Eq. 25. Furthermore, the average wind speed ν_a for the short building and the tall building are selected from the building's respective locations: the Building Standard Law of Japan (BSLJ-2000) (Tamura et al. 2004) for the short building and ASCE 7-10 (Table C26.5-3) (ASCE 2013) for the tall building.

Four wind speed time series are generated: two having a wind speed gust component ω_g from the expression for $\nu_{\text{gust}}(t)$ acting at the first natural frequency of each structure, and two acting at the second natural frequency of each structure. These first two frequencies are selected due to their large effective modal

mass (Table 4 and 7). The model parameters value are listed in Table 9. Figure 6 shows the wind speed time series simulated around the first natural frequency of each structure. Each time series is produced at a sampling rate of 10 Hz over a 10-minute duration.

TABLE 9: Wind speed model parameters

parameter	short building	tall building
ν_a	32 m/s	63 m/s
A_{ramp}	3 m/s	3 m/s
A_{gust}	-2 m/s	-2 m/s
T_{sr}	50 s	50 s
T_{er}	150 s	150 s
T_{sg}	100 s	100 s
T_{eg}	250 s	250 s
h	40 m	170 m
l	600 m	600 m
z_0	2 m	2 m
N_ω	2^{13}	2^{13}
ω_c	20π rad/s	20π rad/s

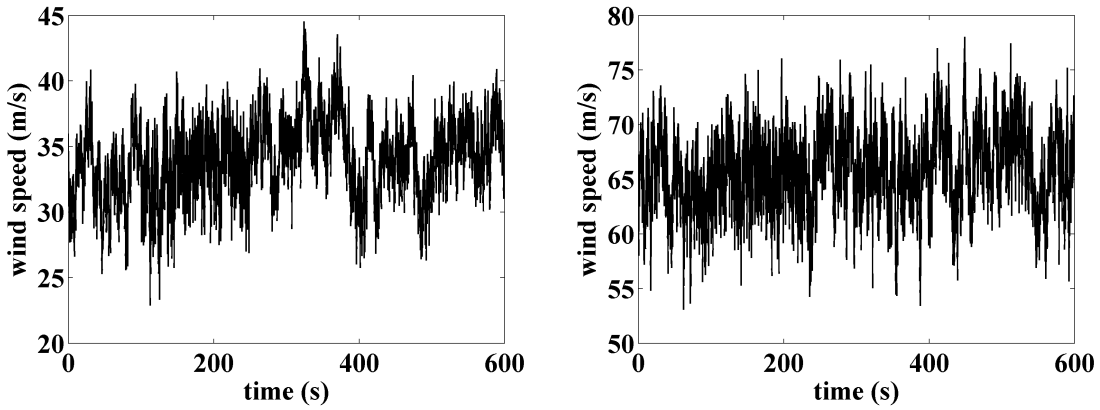

(a) (b)

FIG. 6: Typical realization of a wind time series at a 10 Hz sampling rate over a 10-minute duration : (a) Shizuoka City (top story : 40 m), Japan; and (b) Boston (top story : 170 m), MA.

Finally, the wind load input $u_{w,i}(t)$ at story i is generated from Morrison's equation (Yang et al. 2004)

based on wind speeds obtained from Eq. 25:

$$u_{w,i}(t) = 0.5\rho\nu_{w,i}(t)^2 A_i C_p \tag{26}$$

where ρ is the air density and C_p the combined pressure coefficient, taken as 0.8 (ASCE 7-10, Figure 27.4-1) (ASCE 2013), and A_i is vertical area of floor i.

Blast Load

The simulated blast load is a blast pressure wave, as illustrated in Fig. 7 (Ngo et al. 2007). At the beginning of the explosion, the air pressure builds up quickly to the peak pressure value $P_{\max}$ and remains positive for a duration t_d before dropping negative for a duration t_n.

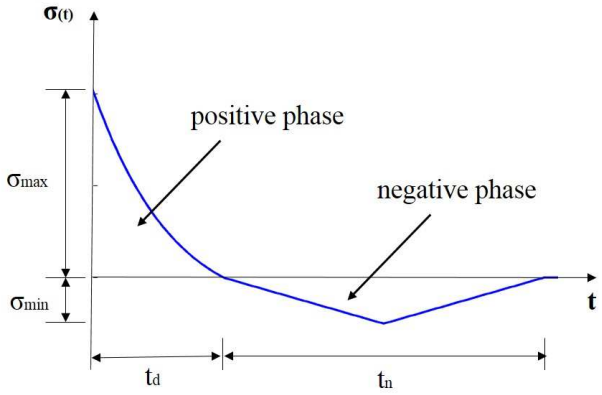

FIG. 7: Time history of an air blast wave pressure

The positive phase ($t < t_d$), is simulated using the general descending pulse model (Li and Meng 2002)

$$P(t) = P_{\max}\left(1 - \lambda_b \frac{t}{t_d}\right) e^{-\gamma_b \frac{t}{t_d}} \tag{27}$$

and the negative phase ($t_d < t < t_d + t_n$) approximated by a bilinear equation (Larcher 2008)

$$P(t) = \begin{cases} -2P_{\min}\frac{t-t_d}{t_n} & \text{if} \quad t_d < t < t_d + t_n/2 \\ -2P_{\min}\frac{t_d+t_n-t}{t_n} & \text{if} \quad t_d + t_n/2 < t < t_d + t_n \end{cases} \tag{28}$$

These functions were used to produce Fig. 7. The blast load parameters are selected based on the 1995 Oklahoma City bombing event (Mendis et al. 2002). They are listed in Table 10. The blast load distribution on each building follows the example provided in the literature (Ngo et al. 2007), where only the first seven floors are affected (or all floors in the case of the short building). The peak pressure value $P_{\max}$ at each floor is obtained by linear interpolation. These values are listed in Table 11. The blast load is simulated

to provide insight on whether a semi-active system may have potential at mitigating a high impulse load. In applications, it would be important to assess the effect of delays between the excitation, sensors, and mechanical feedback.

TABLE 10: Model parameters from Oklahoma bombing of 1995

parameter	value
$P_{\max}$	4100 Kpa
$P_{\min}$	10 Kpa
R	20 m
W	1814 Kg
λ_b	1
γ_b	2.8
t_d	15 ms
t_n	134 ms

TABLE 11: Peak pressure value $P_{\max}$ for simulated building

floor	short building		tall building	
number	height (m)	$P_{\max}$ (kPa)	height (m)	$P_{\max}$ (kPa)
1	4.2	4100	4.57	4100
2	7.8	1762	12.19	522
3	11.4	642	18.28	46
4	15	156	22.24	16
5	18.6	36	26.2	9
6	NA	NA	30.16	6
7	NA	NA	34.12	1

Seismic Loads

A set of six different earthquakes were used to simulate seismic excitations. They were selected due to their different dynamic characteristics, including the impulses and epicentral distances. They are listed in Table 12. Near-field and far-field earthquakes are defined based on the epicentral distance, where 0 to 50 km is considered as near-field and 50 km and beyond is considered as far-field.

TABLE 12: List of simulated earthquakes

	location	year	station	dist(km)	mechanism	mag.(RS)
near-field	Kobe, Japan	1995	Nishi-Akashi	7.1	strike-slip	6.9
	San Francisco, CA	1957	Golden Gate Park	9.6	reverse	5.28
	Imperial Valley, CA	1940	El Centro Array 9	13	strike-slip	7
far-field	Loma Prieta, CA	1989	Oakland Title	72.1	reverse-oblique	6.93
	Chi-Chi, Taiwan	1999	CHY012	59	reverse-oblique	7.62
	Big Bear City, CA	2003	Caltech Millikan Library	118	strike-slip	4.92

Each ground motions was scaled to the target response spectra based on the amplitude-scaling method (Bazzurro and Luco 2004). The local design response spectra of the short and tall building were established using the USGS seismic design map. Only uni-directional horizontal ground motions were considered. Two design response spectrum are plotted by spectral acceleration parameters S_{DS} and S_{D1} based on ASCE 7-10 (ASCE 2013). Values for S_{DS} and S_{D1} for the short building were obtained by extracting S_1 and S_s parameters in Japan from the USGS website and computing S_{DS} and S_{D1} following ASCE 7-10 section 11.4 (ASCE 2013). Values for S_{DS} and S_{D1} for the tall building were obtained directly from the USGS website using the building locations. These parameters are listed in Table 13. The scale factor of the six ground motions are calculated by the PEER ground motion record database (PEER 2010). They are listed in Table 14.

TABLE 13: Design spectral acceleration parameters

	short building	tall building
S_{DS}	1.52 g	0.229 g
S_{D1}	0.91 g	0.11 g

TABLE 14: Scale factor of selected ground motions

	short building	tall building
Kobe	2.91	1.70
San Francisco	65.72	83.28
Imperial Valley	1.93	1.29
Loma Prieta	2.48	1.73
Chi-Chi	8.41	0.56
Big Bear City	45.30	69.20

The scaled ground motion response spectrum for two selected building are plotted in Figure 8 and all six ground motions match the target spectrum at the fundamental period of each building (0.992 sec for the short building and 5.28 sec for the tall building).

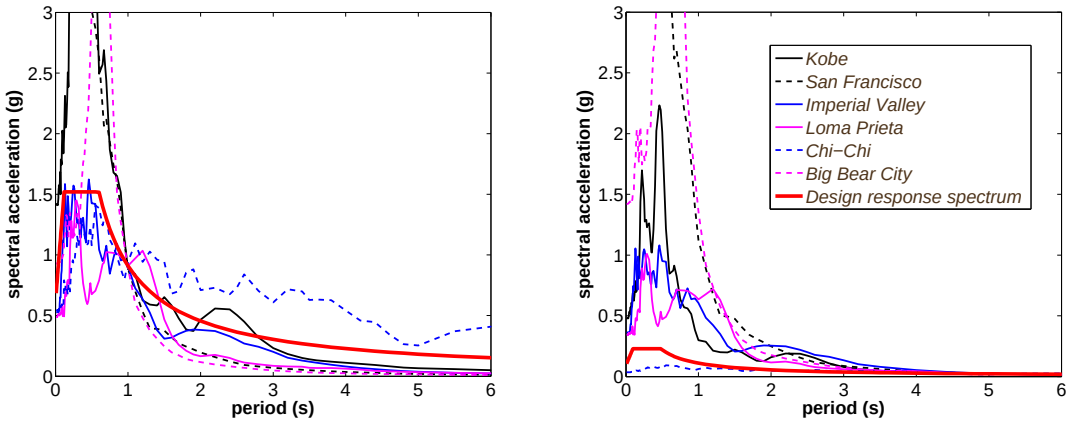

(a) (b)

FIG. 8: Scaled response spectra of selected ground motions : (a) short building, Japan (fundamental period $\omega_1 = 0.992$ sec); and (b) tall building, MA (fundamental period $\omega_1 = 5.28$ sec).

Simulation Cases

Each hazard listed above is simulated individually on each structure. Simulation cases include the uncontrolled case for the performance benchmark, the passive viscous case using capacities listed in Table 5 and 8, friction control cases (VISC and FRIC), where the passive friction case includes the dynamics of the MFD without backlash (as illustrated by the blue line in Fig. 3), the passive-on case (ON), where the MFD is continuously set to its maximum friction force (i.e., full voltage), and five SMC cases each using a

different set of control weight parameters (SMC1 to SMC5), listed in Table 15. These weights were selected arbitrarily to provide a wide range of possible performance, without pre-tuning. Note that the design of an optimal controller is out-of-the-scope of this paper.

TABLE 15: Sliding mode control cases

simulation	short building		tall building	
case	λ	η	λ	η
SMC1	1	50	0.1	5
SMC2	1	100	2	5
SMC3	10	100	0.01	5
SMC4	10	150	1	3
SMC5	100	150	0.5	10

The simulated loads are named as follows: wind1 and wind2, which are the wind loads time series with dominating frequencies around the first (wind1) and second (wind2) frequencies of each building, blast, which is the blast load, EQ1 to EQ6, which correspond to the Kobe, San Francisco, Imperial Valley, Loma Prieta, Chi-chi, and Big Bear City earthquakes, respectively.

SIMULATION RESULTS AND DISCUSSIONS

Simulation results presented in this section are compared using the following four performance indices:

- Maximum drift reduction J_1

$$J_1 = \frac{\max_{i,t}|x_{\mathrm{unc},i}(t)| - \max_{i,t}|x_i(t)|}{\max_{i,t}|x_{\mathrm{unc},i}(t)|} \tag{29}$$

  where x_i is the controlled inter-story state, and $x_{\mathrm{unc},i}$ is the uncontrolled inter-story state.

- Maximum absolute acceleration reduction J_2

$$J_2 = \frac{\max_{i,t}|\ddot{z}_{\mathrm{unc},i}(t)| - \max_{i,t}|\ddot{z}_i(t)|}{\max_{i,t}|\ddot{z}_{\mathrm{unc},i}(t)|} \tag{30}$$

  where $\ddot{z}_i$ is the controlled acceleration state, and $\ddot{z}_{\mathrm{unc},i}$ is the uncontrolled acceleration state.

- Base shear reduction J_3

$$J_3 = \frac{\max_t|V_{\mathrm{unc,base}}(t)| - \max_t|V_{\mathrm{base}}(t)|}{\max_t|V_{\mathrm{unc,base}}(t)|} \tag{31}$$

  where $V_{\mathrm{base}}(t)$ is controlled base shear, and $V_{\mathrm{unc,base}}$ is the uncontrolled base shear.

TABLE 16: Best control case and performance index value per hazard and building type

(a) short building

hazard	J1			J2			J3		
	case	value (%)	IP (%)	case	value (%)	IP (%)	case	value (%)	IP (%)
wind1	SMC3	62.3	0.46	SMC1	72.9	0.14	SMC5	81.6	1.62
wind2	SMC4	41.4	2.35	SMC3	37.5	12.9	SMC3	47.5	4.87
blast	VISC	2.71	0.19	VISC	14.6	1.40	VISC	0.05	0.01
EQ1	SMC4	45.9	0.17	SMC2	24.9	0.05	SMC4	26.8	0.18
EQ2	SMC2	25.8	1.48	SMC2	10.8	0.28	SMC2	6.73	0.12
EQ3	FRIC	82.6	11.2	SMC3	51.6	2.60	SMC5	55.3	0.43
EQ4	SMC4	79.9	0.19	SMC4	61.1	14.8	SMC4	70.2	1.45
EQ5	FRIC	73.1	1.46	SMC4	59.1	2.45	SMC4	64.2	3.79
EQ6	VISC	25.2	4.33	SMC5	13.1	0.14	SMC5	16.7	0.08

(b) tall building

hazard	J1			J2			J3		
	case	value (%)	IP (%)	case	value (%)	IP (%)	case	value (%)	IP (%)
wind1	SMC2	42.6	17.0	SMC2	46.0	12.3	SMC2	63.4	9.41
wind2	SMC4	9.33	2.06	SMC2	16.7	0.99	SMC2	26.8	5.02
blast	SMC1	43.5	0.01	SMC2	44.9	0.01	SMC3	40.3	0.01
EQ1	SMC2	10.1	4.93	VISC	-0.37	0.11	VISC	-0.57	0.16
EQ2	SMC4	6.85	3.80	VISC	-0.03	0.22	SMC2	0.38	0.02
EQ3	SMC2	58.1	0.57	SMC2	47.3	1.41	VISC	-1.54	2.93
EQ4	SMC2	38.4	2.01	SMC2	16.2	4.93	VISC	-0.47	0.32
EQ5	SMC4	53.9	4.38	SMC4	51.4	6.75	SMC2	31.5	5.71
EQ6	SMC5	15.4	0.35	SMC2	1.62	0.19	SMC2	1.09	0.32

- Average voltage use J_4

$$J_4 = \frac{1}{v_b N} \sum_{i}^{N} \left(\frac{1}{t} \int_0^t v_i dt \right) \tag{32}$$

where v_b is the voltage bound ($v_b = 12$ v), and N is the number of devices for the entire building.

The performance indices J_1 to J_4 are shown in Figs. 9 and 10 for the short and the tall building, respectively. Table 16 lists the best control strategies in term of mitigation performance under each hazard, along with the value of each associated performance indices and the improvement in performance (IP) with respect to the second best control strategy for each individual performance measure. This performance measure can be used to assess whether there exist a controller that performs significantly better than other controllers.

The comparison of the overall mitigation performances for all control strategies across all hazards show that no single control solution is optimal, as one would expect given the different dynamic inputs under study. For the short building, a friction mechanism typically outperforms the passive viscous strategy for performance indices J_1 to J_3 in most cases, except for blast mitigation where it outperformed all strategies at

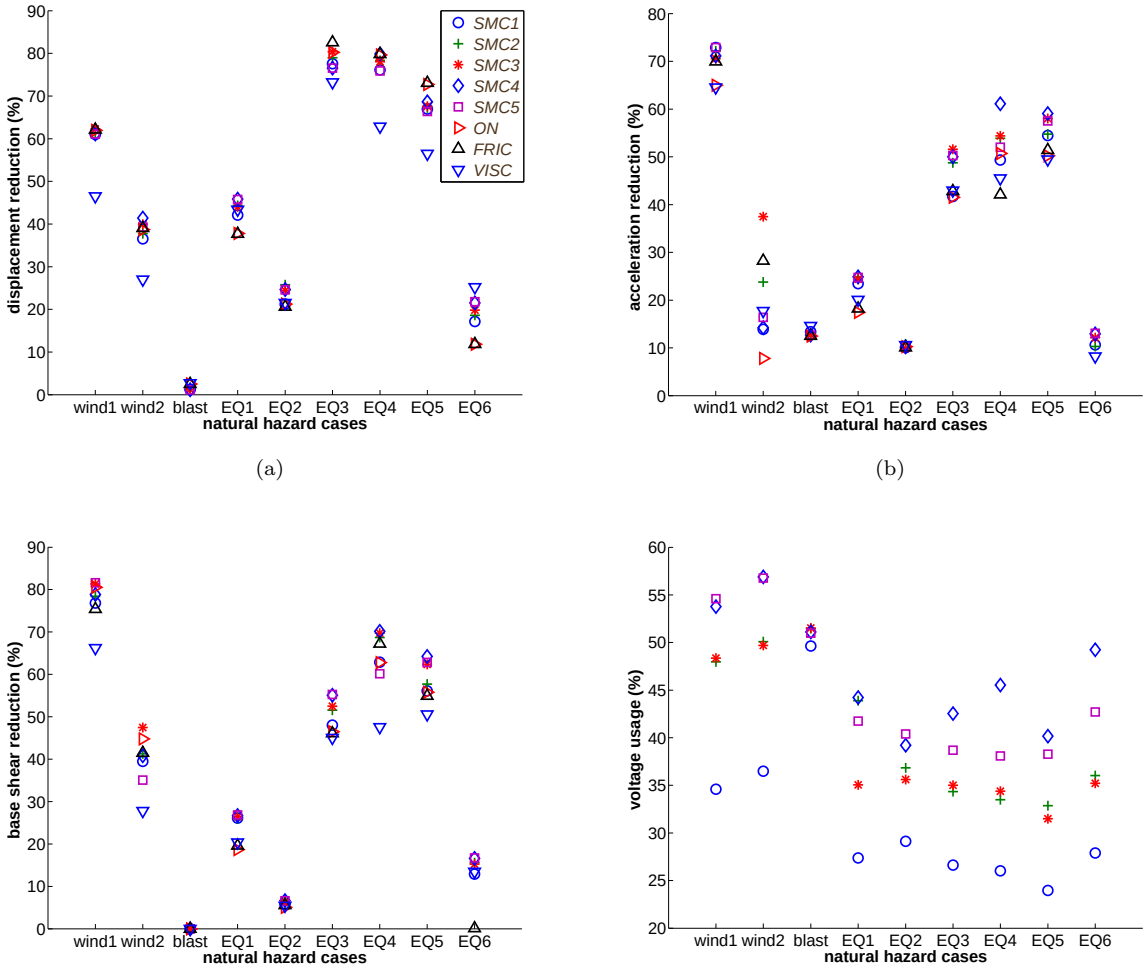

FIG. 9: Performance of controlled short building under multi-hazard excitation : (a) J_1; (b) J_2; (c) J_3; and (d) J_4.

mitigating displacement and acceleration for the short building. However, such performance is not significant compared with other strategies, which can be attributed to the overall rigidity of the building. A look at the blast mitigation for the tall structure shows that the passive viscous strategy significantly underperforms all other cases. Nevertheless, all of these other control cases do not show significant difference in performance. The passive viscous strategies provides very low mitigation performance overall for the tall structure.

A comparison of results with the passive friction case shows that passive friction provides a better displacement mitigation performance (J_1) for some of the earthquake loads (EQ3 and EQ5) for the short building, but does not appear to outperform any of the semi-active control cases for other hazards. A comparison of the passive friction performance with the passive-on case provides an insight on the effects

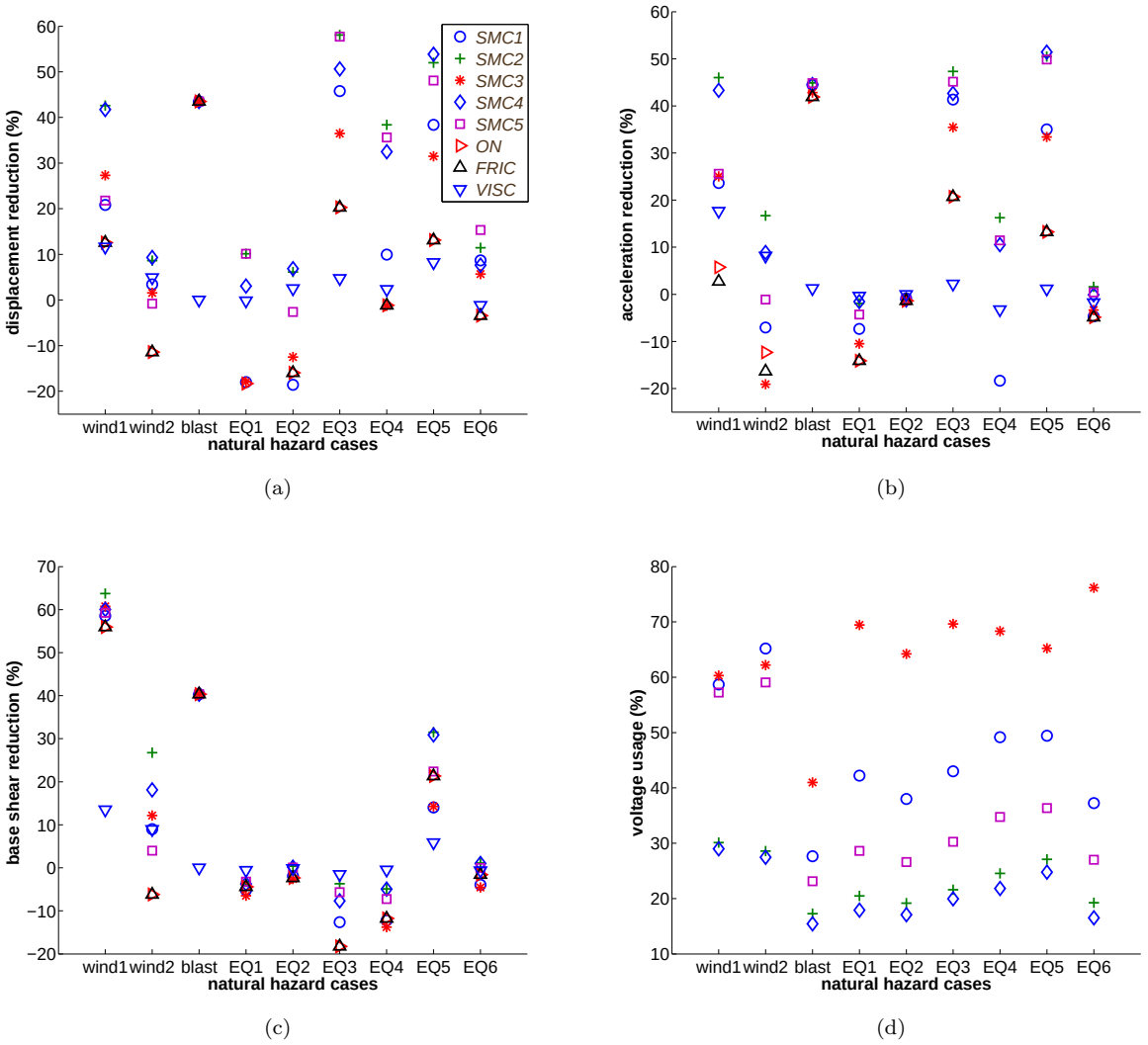

FIG. 10: Performance of controlled tall building under multi-hazard excitation : (a) J_1; (b) J_2; (c) J_3; and (d) J_4.

of the backlash mechanism (Fig. 3). Results shows that the passive friction strategy has similar mitigation performance compare with the passive-on case, except for wind mitigation for the tall structure. This is due to the higher drifts found in the tall building subjected to wind, which results in a more negligible effect of the backlash mechanism. It can also be observed that the passive friction mechanism worsens structural response under wind2, EQ1 and EQ2 for the tall structure due to the shift in the response function provoked by the added stiffness. In these situations, control is necessary to ensure a reduction in responses. This is also the case for some passive-on strategies in particular, for the J_2 index for the tall building.

Results also show that semi-active control (SMC1-SMC5) performs as well or better than all other strategies under performance indices J_1 to J_3, except for J_1 under hazards EQ3 and EQ6 for the short

building, and J_3 under hazards EQ3 and EQ4 for the tall building, see Table 16. These results demonstrate that the MFD could be used at effectively mitigating different hazards. However, a closer look at the semi-active control cases (SMC1-SMC5) shows that no single controller dominates performance over all hazards. Some control weights are more appropriate for given excitations. This is also expected given that each set of excitations have different dynamic properties (e.g., magnitude, frequency content).

An investigation of performance J_4 gives insights on the overall cost (voltage) required for each control strategy. All control weight cases are mostly consistently ranked in terms of voltage requirement over all hazards, for both the short and tall buildings. But this ranking is not constant between both types of buildings. There is no clear relationship between the average voltage and the mitigation performance. Results from this performance index can be used to further study the mitigation efficiency of each control strategy. Figures 11 and 12 show the mitigation performance for indices J_1 and J_2 divided by the average voltage utilization for the short and the tall building, respectively, providing a unitless measure of efficiency. For the short building, the control weights resulting in the smallest voltage usage (SMC1 in Fig. 9(d)) resulted in a better efficiency with respect to other control cases for all hazards, except wind2 under J_2. This is also the case for the tall structure, but with SMC4. These results demonstrate a diminished gain in performance with increasing voltage usage. However, given the typical low power requirement of semi-active devices (the MFD was designed to function on a car battery), more aggressive control strategies could be more appropriate.

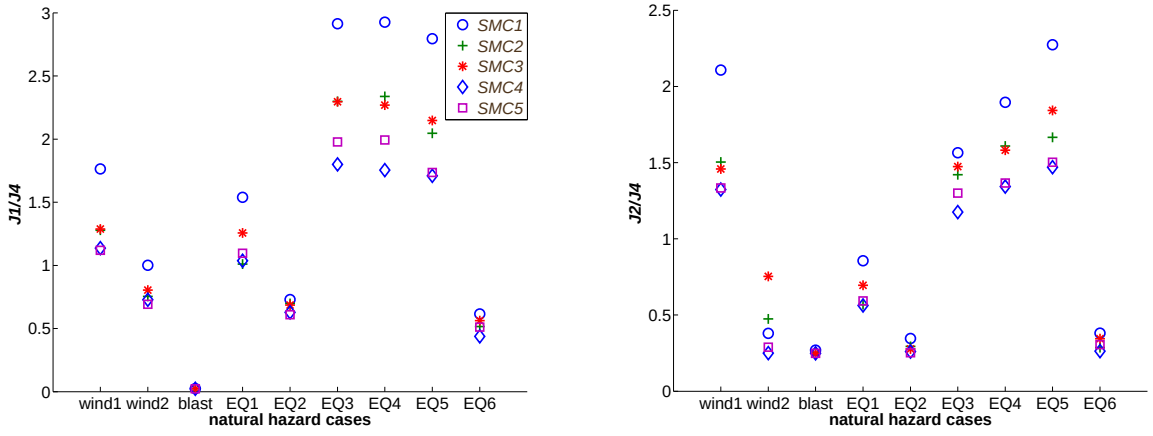

(a) (b)

FIG. 11: Performance index ratio of controlled short building under multi-hazard excitation : (a) J_1/J_4;and (b) J_2/J_4.

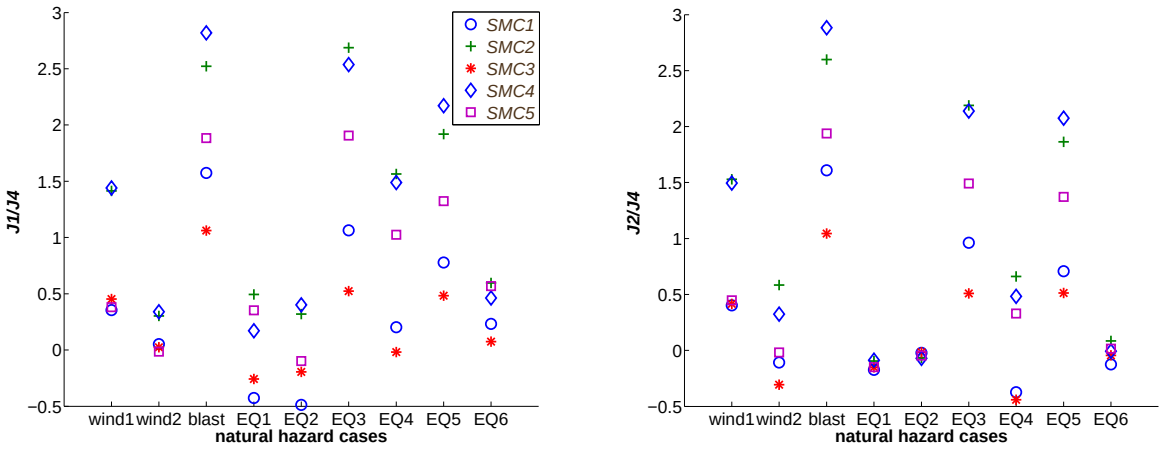

(a) (b)

FIG. 12: Performance index ratio of controlled tall building under multi-hazard excitation : (a) J_1/J_4; and (b) J_2/J_4.

The effect of the backlash mechanism is further investigated by comparing mitigation results with an hypothetical device that would have an ideal friction behavior, as illustrated in Fig. 3. Table 17 list the mitigation results for performance indices J_1 to J_3 using the control gains (cases SMC1 to SMC5) that provided the best semi-active mitigation results under each individual measure. Results are compared in terms of improvement in performance (IP) relative to each best semi-active control base. An ideal friction dynamic behavior generally provides better mitigation performance. In some cases, this improvement is not significant, or there is a slight loss in performance. In two particular cases (wind2 and EQ4 for the short building), the ideal friction dynamic results in a significant loss in acceleration (J_2) and base shear (J_3) mitigation performance. This is likely due to the slower change in the device's dynamic upon motion reversal, as mentioned earlier.

TABLE 17: performance indices and improvement percentage (IP) of pure LuGre model simulation with best control case

hazard	short building						tall building					
	J1	IP (%)	J2	IP (%)	J3	IP (%)	J1	IP (%)	J2	IP (%)	J3	IP (%)
wind1	62.2	-0.35	80.6	33.8	84.0	14.1	42.1	-0.91	47.6	2.95	64.5	2.14
wind2	39.2	-1.23	25.9	-18.5	39.3	-15.6	9.93	0.66	14.7	-2.36	19.8	-9.47
blast	1.29	0.08	13.8	0.43	1.00	0.01	43.5	0.01	45.2	0.62	40.4	0.01
EQ1	45.3	-1.06	24.5	-0.53	24.8	-2.54	11.30	1.32	-0.26	-3.62	-2.99	-2.40
EQ2	24.9	-1.10	11.3	0.52	6.63	-0.12	6.97	0.12	-1.21	-1.17	0.17	-0.22
EQ3	81.2	3.91	53.0	2.92	53.2	1.43	58.6	1.24	47.4	0.13	-3.76	-2.18
EQ4	81.5	7.98	46.9	-36.5	60.4	-32.7	38.9	0.84	16.8	0.61	-4.85	-4.35
EQ5	73.8	16.3	61.4	5.68	67.9	10.2	54.7	1.82	52.3	1.88	30.9	-0.93
EQ6	21.3	-0.64	11.4	-1.92	15.3	-1.68	15.0	-0.45	0.39	-1.25	-0.30	-1.40

SUMMARY AND CONCLUSIONS

In this paper, numerical simulations were conducted to investigate the performance of a novel semi-active damping device at multi-hazard mitigation. The device, termed modified friction device (MFD), is a variable friction device based on automotive drum brake technology. An important dynamic feature of the device is a backlash mechanism, which results in an important drop in the friction force upon motion reversal due to gaps in the mechanical components. The MFD has been previously tested in a laboratory environment and a 3-stage dynamic model developed that characterized its dynamic behavior. This model was used in the numerical simulations. Simulations consisted of two representative building: one short structure (5 story) located in Japan, and one tall structure (39 storys) located in Boston, MA. Hazards under consideration included two wind loads acting on the first and second natural frequencies of the structures, one blast load, and six different seismic loads. Both structures were virtually equipped with MFDs, passive viscous, or passive friction devices. Performance-based design procedures were used to simulate devices of similar dynamic capacities. Five different sliding mode control (SMC) cases were considered, which consistent of non-optimized control weights.

Results show that, in the vast majority of hazards, one semi-active control case provided the best mitigation performance for reducing interstory displacement, acceleration, and base shear. This demonstrated that the MFD could be used to effectively mitigate all hazards, provided that the right control weights were utilized. In a passive mode, the presence of the backlash mechanism resulted in a loss of efficiency, except for mitigation of wind load for flexible structures, where the device's displacement is large enough to mini-

mize the effect of the backlash mechanism. A study of control efficiency, defined as mitigation performance divided by the average voltage usage, showed that the gain in mitigation performance diminished with the voltage input. The effect of such trade-off is minimized for the MFD given its low voltage requirement. An investigation of the effect of the backlash mechanism was studied in a control mode by comparing mitigation performance versus a similar device with ideal friction dynamics. It was found that in most cases, the presence of the backlash resulted in sub-optimal performances.

In summary, findings from this study demonstrated the potential of the device at mitigating multiple non-simultaneous hazards. The device itself could be improved by designing a mechanism that minimizes the backlash. To fully enable the full potential of the device, it is critical to develop adaptive controllers capable of adapting the control rules to provide optimal performance under different hazards.

ACKNOWLEDGEMENTS

This material is based upon work supported by the National Science Foundation under Grant No. 1300960. Their support is gratefully acknowledged. Any opinions, findings, and conclusions or recommendations expressed in this material are those of the author(s) and do not necessarily reflect the views of the National Science Foundation.

REFERENCES

Agrawal, A. K. and Yang, J. N. (2000). "Semiactive control strategies for buildings subject to near field earthquakes." International Society for Optics and Photonics, 359–370.

ASCE (2013). Minimum Design Loads for Buildings and Other Structures. American Society of Civil Engineers, Reston, VA, asce/sei 7-10 edition.

Asprone, D., Jalayer, F., Prota, A., and Manfredi, G. (2010). "Proposal of a probabilistic model for multi-hazard risk assessment of structures in seismic zones subjected to blast for the limit state of collapse." Structural Safety, 32(1), 25–34.

Bazzurro, P. and Luco, N. (2004). "Parameterization of non-stationary acceleration time histories." Lifelines Program Project 1G00 Addenda.

Cao, L., Downey, A., Laflamme, S., Taylor, D., and Ricles, J. (2015),). "Variable friction device for structural control based on duo-servo vehicle brake: Modeling and experimental validation." J. Sound and Vibration.

Casciati, F., Rodellar, J., and Yildirim, U. (2012). "Active and semi-active control of structures–theory and applications: A review of recent advances." Journal of Intelligent Material Systems and Structures, 1045389X12445029.

Chen, C. and Chen, G. (2004). "Shake table tests of a quarter-scale three-storey building model with piezoelectric friction dampers." Structural Control and Health Monitoring, 11(4), 239–257.

Connor, J. J. and Laflamme, S. (2014). Structural Motion Engineering. Springer.

Constantinou, M. C., Tsopelas, P., Hammel, W., and Sigaher, A. N. (2001). "Toggle-brace-damper seismic energy dissipation systems." Journal of Structural Engineering, 127(2), 105–112.

Dai, H., Liu, Z., and Wang, W. (2012). "Structural passive control on electromagnetic friction energy dissipation device." Thin-Walled Structures, 58, 1–8.

Dong, Y., Frangopol, D. M., and Saydam, D. (2013). "Time-variant sustainability assessment of seismically vulnerable bridges subjected to multiple hazards." Earthquake Engineering & Structural Dynamics, 42(10), 1451–1467.

Durmaz, O., Clark, W. W., Bennett, D. S., Paine, J. S., and Samuelson, M. N. (2002). "Experimental and analytical studies of a novel semi-active piezoelectric coulomb damper." SPIE's 9th Annual International Symposium on Smart Structures and Materials, International Society for Optics and Photonics, 258–273.

Ganzerli, S., Pantelides, C., and Reaveley, L. (2000). "Performance-based design using structural optimization." Earthquake engineering & structural dynamics, 29(11), 1677–1690.

Hsu, S., Meindl, E. A., and Gilhousen, D. B. (1994). "Determining the power-law wind-profile exponent under near-neutral stability conditions at sea." Journal of Applied Meteorology, 33(6), 757–765.

Iyama, J., Seo, C., Ricles, J., and Sause, R. (2009). "Self-centering mrfs with bottom flange friction devices under earthquake loading." Journal of Constructional Steel Research, 65(2), 314–325.

Jalayer, F., Asprone, D., Prota, A., and Manfredi, G. (2011). "Multi-hazard upgrade decision making for critical infrastructure based on life-cycle cost criteria." Earthquake Engineering & Structural Dynamics, 40(10), 1163–1179.

Kannan, S., Uras, H. M., and Aktan, H. M. (1995). "Active control of building seismic response by energy dissipation." Earthquake engineering & structural dynamics, 24(5), 747–759.

Kawamoto, Y., Suda, Y., Inoue, H., and Kondo, T. (2008). "Electro-mechanical suspension system considering energy consumption and vehicle manoeuvre." Vehicle System Dynamics, 46(1), 1053–1063.

Kurata, N., Kobori, T., Takahashi, M., Niwa, N., and Midorikawa, H. (1999). "Actual seismic response controlled building with semi-active damper system. earthquake engineering and structural dynamics." John Wiley & Sons, 28(11), 1427–1447.

Laflamme, S. et al.(2011a). "Control of large-scale structures with large uncertainties." Ph.D. thesis, Massachusetts Institute of Technology, Massachusetts Institute of Technology.

Laflamme, S., Slotine, J., and Connor, J. (2011b). "Wavelet network for semi-active control." Journal of Engineering Mechanics, 137(7), 462–474.

Laflamme, S., Slotine, J. E., and Connor, J. (2012a). "Self-organizing input space for control of structures." Smart Materials and Structures, 21(11), 115015.

Laflamme, S., Taylor, D., Abdellaoui Maane, M., and Connor, J. J. (2012b). "Modified friction device for control of large-scale systems." Structural control and health monitoring, 19(4), 548–564.

Larcher, M. (2008). "Pressure-time functions for the description of air blast waves." JRC Technical Note, (46829).

Li, Q. and Meng, H. (2002). "Pressure-impulse diagram for blast loads based on dimensional analysis and single-degree-of-freedom model." Journal of engineering mechanics, 128(1), 87–92.

Lorenz, M., Heimann, B., and Härtel, V. (2006). "A novel engine mount with semi-active dry friction damping." Shock and Vibration, 13(4), 559–571.

Lu, L.-Y. and Lin, G.-L. (2009). "A theoretical study on piezoelectric smart isolation system for seismic protection of equipment in near-fault areas." Journal of Intelligent Material Systems and Structures, 20(2), 217–232.

Mahmoud, K. R. M. (2005). Theoretical and experimental investigations on a new adaptive duo servo drum brake with high and constant brake shoe factor. HNI.

McCullough, M. and Kareem, A. (2011). "A framework for performance-based engineering in multi-hazard coastal environments." Proceedings of the 2011 Structures Congress, Las Vegas, USA, April, 14-16 2011.

McNamara, R., Huang, C., and Wan, V. (2000). "Viscous-damper with motion amplification device for high rise building applications." Proceedings of the 2000 Structures Congress & Exposition.

Mcnamara, R. J. and Taylor, D. P. (2003). "Fluid viscous dampers for high-rise buildings." The structural design of tall and special buildings, 12(2), 145–154.

Mehmood, A., Laghrouche, S., and El Bagdouri, M. (2011). "Modeling identification and simulation of pneumatic actuator for vgt system." Sensors and Actuators A: Physical, 165(2), 367–378.

Mendis, P., Ngo, T., Haritos, N., Hira, A., Samali, B., and Cheung, J. (2007). "Wind loading on tall buildings." EJSE Special Issue: Loading on Structures, 3, 41–54.

Mendis, P., Ngo, T., and Kusuma, G. (2002). "Assessment of tall buildings under blast loading and aircraft impact." Invited paper-Seminar The Future for Concrete Tall buildings following September, Vol. 11.

Mualla, I. H. and Belev, B. (2002). "Performance of steel frames with a new friction damper device under earthquake excitation." Engineering Structures, 24(3), 365–371.

Narasimhan, S. and Nagarajaiah, S. (2006). "Smart base isolated buildings with variable friction systems: H controller and saivf device." Earthquake engineering & structural dynamics, 35(8), 921–942.

Ngo, T., Mendis, P., Gupta, A., and Ramsay, J. (2007). "Blast loading and blast effects on structures–an overview." Electronic Journal of Structural Engineering, 7, 76–91.

PEER (2010). "Peer, pacific earthquake engineering research center.

Petrini, F. and Palmeri, A. (2012). "Performance-based design of bridge structures subjected to multiple

hazards: a review." 6th International Conference on Bridge Maintenance, Safety and Management, 2040–2047.

Ricles, J., Sause, R., Peng, S., and Lu, L. (2002). "Experimental evaluation of earthquake resistant posttensioned steel connections." Journal of Structural Engineering, 128(7), 850–859.

Seo, C.-Y. and Sause, R. (2005). "Ductility demands on self-centering systems under earthquake loading." ACI Structural Journal, 102(2).

Shinozuka, M. and Jan, C.-M. (1972). "Digital simulation of random processes and its applications." Journal of sound and vibration, 25(1), 111–128.

Slootweg, J., De Haan, S., Polinder, H., and Kling, W. (2003). "General model for representing variable speed wind turbines in power system dynamics simulations." Power Systems, IEEE Transactions on, 18(1), 144–151.

Spencer Jr, B. and Nagarajaiah, S. (2003). "State of the art of structural control." Journal of structural engineering, 129(7), 845–856.

Stewart, J. P., Chiou, S.-J., Bray, J. D., Graves, R. W., Somerville, P. G., and Abrahamson, N. A. (2002). "Ground motion evaluation procedures for performance-based design." Soil dynamics and earthquake engineering, 22(9), 765–772.

Symans, M., Charney, F., Whittaker, A., Constantinou, M., Kircher, C., Johnson, M., and McNamara, R. (2008). "Energy dissipation systems for seismic applications: current practice and recent developments." Journal of structural engineering, 134(1), 3–21.

Takewaki, I. (2011). Building control with passive dampers: optimal performance-based design for earthquakes. John Wiley & Sons.

Tamura, Y., Kawai, H., Uematsu, Y., Okada, H., and Ohkuma, T. (2004). "Documents for wind resistant design of buildings in japan." Workshop on Regional Harmonization of Wind Loading and Wind Environmental Specifications in Asia-Pacific Economies (APEC-WW), 61–84.

Trifunac, M. D. (2012). "Earthquake response spectra for performance based designa critical review." Soil Dynamics and Earthquake Engineering, 37, 73–83.

Ubertini, F. (2010). "Prevention of suspension bridge flutter using multiple tuned mass dampers." Wind and Structures, 13(3), 235–256.

Ubertini, F., Comanducci, G., and Laflamme, S. (2015). "A parametric study on reliability-based tuned-mass damper design against bridge flutter." Journal of Vibration and Control, 1077546315595304.

Ubertini, F. and Giuliano, F. (2010). "Computer simulation of stochastic wind velocity fields for structural response analysis: Comparisons and applications." Advances in Civil Engineering, 2010(749578), 1–20.

Venanzi, I., Ubertini, F., and Materazzi, A. L. (2013). "Optimal design of an array of active tuned mass

512 dampers for wind-exposed high-rise buildings." Structural Control and Health Monitoring, 20(6), 903–917.
513 Vesselenyi, T., Dzitac, S., Dzitac, I., and Manolescu, M.-J. (2007). "Fuzzy and neural controllers for a
514 pneumatic actuator." International Journal of Computers, Communications and Control, 2(4), 375–387.
515 Xu, Y. and Ng, C. (2008). "Seismic protection of a building complex using variable friction damper: exper-
516 imental investigation." Journal of engineering mechanics, 134(8), 637–649.
517 Yang, J. N. and Agrawal, A. K. (2002). "Semi-active hybrid control systems for nonlinear buildings against
518 near-field earthquakes." Engineering Structures, 24(3), 271–280.
519 Yang, J. N., Agrawal, A. K., Samali, B., and Wu, J.-C. (2004). "Benchmark problem for response control of
520 wind-excited tall buildings." Journal of Engineering Mechanics, 130(4), 437–446.